ACSNANO

www.acsnano.org

ARTICLE

Chiral Light Emission from a Hybrid Magnetic Molecule–Monolayer Transition Metal Dichalcogenide Heterostructure

Vaibhav Varade, Golam Haider, Artur Slobodeniuk, Richard Korytar, Tomas Novotny, Vaclav Holy, Jiri Miksatko, Jan Plsek, Jan Sykora, Miriam Basova, Martin Zacek, Martin Hof, Martin Kalbac,* and Jana Vejpravova*

Cite This: *ACS Nano* 2023, 17, 2170–2181

Read Online

ACCESS | Metrics & More | Article Recommendations | Supporting Information

ABSTRACT: **Hybrid layered materials assembled from atomically thin crystals and small molecules bring great promises in pushing the current information and quantum technologies beyond the frontiers. We demonstrate here a class of layered valley–spin hybrid (VSH) materials composed of a monolayer two-dimensional (2D) semiconductor and double-decker single molecule magnets (SMMs). We have materialized a VSH prototype by thermal evaporation of terbium bis-phthalocyanine onto a MoS_2 monolayer and revealed its composition and stability by both microscopic and spectroscopic probes. The interaction of the VSH components gives rise to the intersystem crossing of the photogenerated carriers and moderate p-doping of the MoS_2 monolayer, as corroborated by the density functional theory calculations. We further explored the valley contrast by helicity-resolved photoluminescence (PL) microspectroscopy carried out down to liquid helium temperatures and in the presence of the external magnetic field. The most striking feature of the VSH is the enhanced *A* exciton-related valley emission observed at the out-of-resonance condition at room temperature, which we elucidated by the proposed nonradiative energy drain transfer mechanism. Our study thus demonstrates the experimental feasibility and great promises of the ultrathin VSH materials with chiral light emission, operable by physical fields for emerging opto-spintronic, valleytronic, and quantum information concepts.**

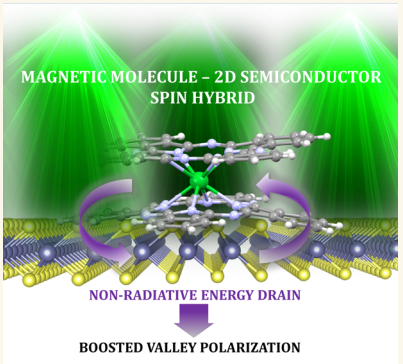

KEYWORDS: *Layered materials, transition metal dichalcogenides, molecular magnets, valley polarization, valley–spin hybrid materials, nonradiative energy drain mechanism*

Two-dimensional (2D) materials have been an intense research focus in the past decade.[1,2] In particular, transition metal dichalcogenides (TMDs) have emerged as a class of 2D materials with promising optical and electronic properties, which offer diverse applications, such as field-effect transistors, nanoscale optoelectronic devices (light-emitting diodes, lasers, and optical detectors) and photonic circuits.[3−6] Moreover, mono- and double-layer TMDs are well-known for their valley-selective physics due to the Berry curvature of the Bloch band acting as an effective magnetic field that induces transverse velocity to charge carriers without the presence of external magnetic fields.[7,8] The consequent transverse responses have been observed in all degrees of freedom of Bloch electrons, including charge, spin, and valley degeneracy, and the latter can be conveniently resolved and studied using circularly polarized (CP) light.[7,8]

One of the most explored TMDs is (1L)MoS_2 with a hexagonal 2H crystal structure and direct band gap in the monolayer (1L) limit, which shows strong and tunable photoluminescence (PL) in the visible region.[9] The variation in the PL of (1L)MoS_2 is not only due to the indirect–direct band gap transition but also influenced by several other factors, including strain, doping, and defect density,[10,11] which are strongly sample dependent and typically vary on the scale of micro- and nanometers within a single flake.[12] Nevertheless, control of the PL via charge transfer by interfacing a TMD with another responsive species has been addressed recently.

A promising strategy is to control the PL with the help of the adsorption of different molecules or quantum dots. For

Received: August 19, 2022
Accepted: January 13, 2023
Published: January 18, 2023

https://doi.org/10.1021/acsnano.2c08320
ACS Nano 2023, 17, 2170–2181

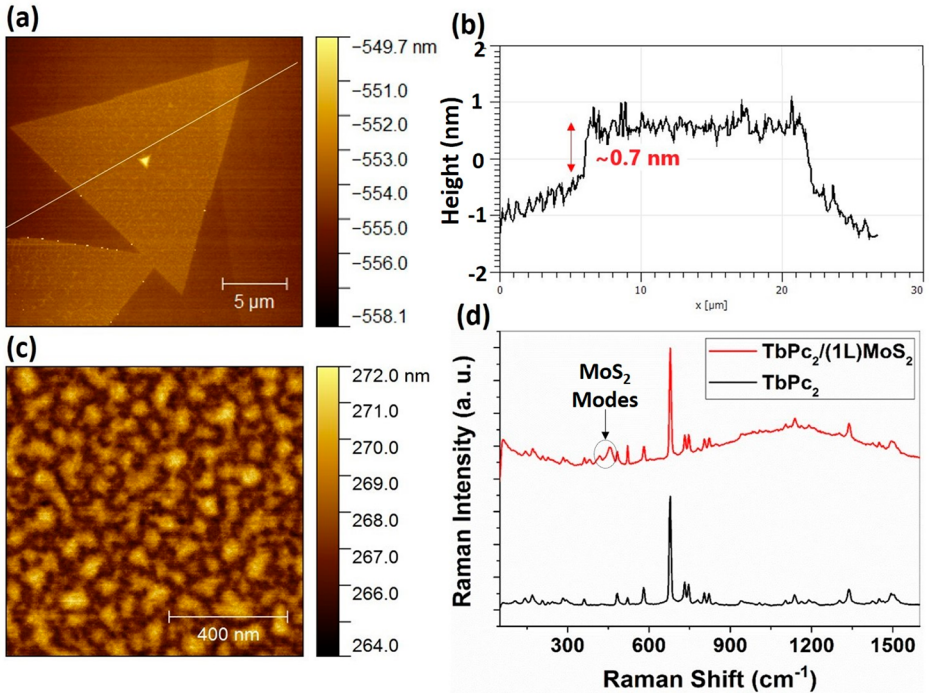

Figure 1. Results of topographic and spectroscopic characterization of (1L)MoS_2 and $TbPc_2$/(1L)MoS_2. (a) A topographical AFM image of (1L)MoS_2 demonstrating a triangular flake shape. The white line crossing the flake corresponds to the sample area depicted for the profile analysis. (b) Thickness profile of (1L)MoS_2 taken along the line shown in panel a. (c) A topographic AFM image of the $TbPc_2$ layer deposited on (1L)MoS_2. (d) Respective Raman spectra of $TbPc_2$ and $TbPc_2$/(1L)MoS_2 VSH (excitation laser energy of 2.33 eV).

example, PL tuning has been demonstrated using organic molecule 3,4,9,10-perylene tetracarboxylic dianhydride.[13] Furthermore, a few experimental and theoretical studies suggested that modulation of the optical and electronic properties of TMDs can be achieved via charge transfer between the TMD and adsorbed π-conjugated organic molecules.[14,15] Therefore, organic π-conjugated metal−phthalocyanines (Pc's) are of particular interest due to their planar structure, convenient for stacking onto the TMD surface, as well as for their electronic, optical, and magnetic tunability, which are functions of the central metal. Such mixed-dimensional heterostructures have attracted reasonable interest.[16,17]

For example, it has been shown that copper phthalocyanine (CuPc) exhibits local enhancement of exciton emission in MoS_2.[18] Weiss and co-workers[19] also reported that the photoinduced charge transfer between CuPc and MoS_2 is strongly dependent on the face-on orientation of CuPc on the (1L)MoS_2 surface. Moreover, the charge separation lasts about 17 times longer than the metal-free Pc/MoS_2.

A very interesting phenomenon occurs on the interface between a (1L)MoS_2 crystal and ZnPc: optically excited singlet exciton in ZnPc transfers to MoS_2, forming a charge-transfer exciton, and singlet−triplet decay occurs due to the large singlet−triplet splitting in ZnPc and strong spin−orbit coupling in MoS_2. The reported spin-selective back electron transfer may enable manipulation of the electron spin in hybrid electronic devices.[20]

Recently, the spin-dependent tunneling barriers, which can be manipulated through modifications of interface coupling, were proposed in mixed heterostructures composed of CoPc and a 2D magnet (VSe_2).[21]

Surprisingly, the interaction of other technologically important classes of magnetic molecules and TMDs has not been addressed. If one takes into account the valley-selective response of (1L)TMDs, coupling of the valley-related pseudospin to another spin entity may result in prospective functionalities within a single hybrid material.

Under this proposition, we selected the terbium(III)bis-(phthalocyaninato) ($TbPc_2$) complex, which is one of the widely studied single molecule magnets (SMMs) with significant importance in the field of quantum information technologies. In standalone $TbPc_2$, a Tb(III) ion is sandwiched between two Pc ligands, and the molecular spin dynamics and magnetization reversal are driven by an energy barrier produced by crystal field splitting of the $J = 6$ ground multiplet.[22] $TbPc_2$ shows strong magnetic anisotropy, with an easy axis of magnetization perpendicular to the Pc plane.[22] However, the interaction of $TbPc_2$ with its surroundings changes the magnetic response dramatically. For example, enhancement of the magnetic bistability of this SMM anchored to the silicon surface was observed,[23] while interaction with magnetic substrates led to a significant reduction of magnetic hysteresis.[24−26] Regarding the interaction of $TbPc_2$ with nanomaterials possessing interesting electronic properties, $TbPc_2$ heterostructures with carbon nanotubes[26,27] and graphene[28,29] have been explored, with a focus on the quantum regime of the SMM emerging at low temperatures.

In this study, we report a prototype of hybrid layered material, a valley−spin hybrid (VSH) system composed of $TbPc_2$ and (1L)MoS_2. We used comprehensive characterization techniques, including optical and photoelectron spectroscopies, to explore the mutual $TbPc_2$/(1L)MoS_2 interaction and the impact of the doping, strain, and defects on the helicity-resolved optical response of the TMD component bearing the valley contrast. We observed a strongly enhanced *A*-exciton-related valley polarization at room temperature, and we proposed a theoretical model to explain

https://doi.org/10.1021/acsnano.2c08320
ACS Nano 2023, 17, 2170−2181

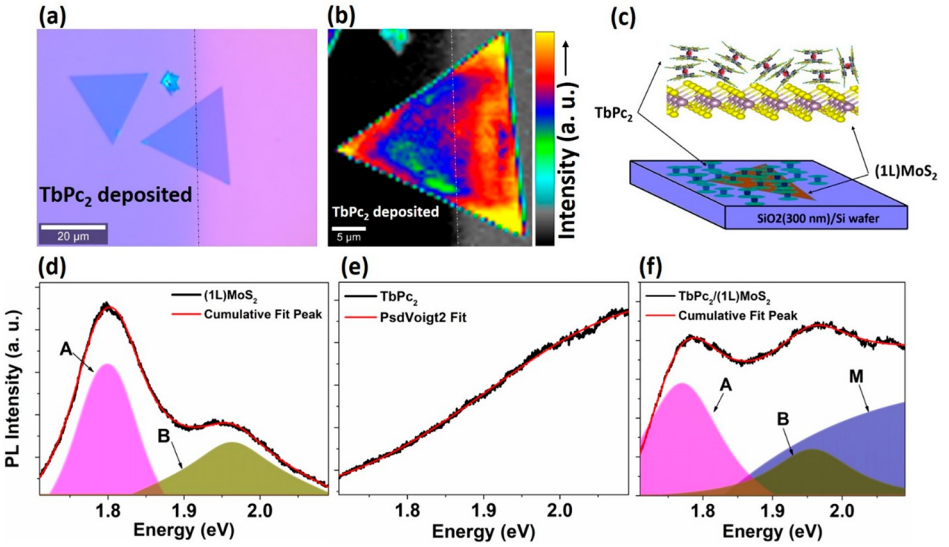

Figure 2. Optical and spectroscopic inspection of the $TbPc_2/(1L)MoS_2$ VSH in comparison to the reference areas. (a) The optical image of $TbPc_2$ deposited on $(1L)MoS_2$. (b) Average PL map depicting $TbPc_2$ covered and noncovered areas on $(1L)MoS_2$ single crystal, with the intensity scale bar. (c) A sketch of $TbPc_2/(1L)MoS_2$ on the SiO_2(300 nm)/Si wafer. The bottom row shows PL spectra (d) for $(1L)MoS_2$, (e) for $TbPc_2$, and (f) for $TbPc_2/(1L)MoS_2$ with the fit using Pseudo−Voigt (PsdVoigt) profile functions, where *A*, *B*, and *M* denote neutral *A* exciton, *B* exciton, and contribution from $TbPc_2$, respectively.

this mechanism. Thus, the mix-dimensional VSH materials show great opportunities thanks to their functionalities, such as chiral light emission revealed already at room temperature.

RESULTS AND DISCUSSION

Preparation and Basic Characterization. First, the $(1L)MoS_2$ flakes were synthesized by chemical vapor deposition (CVD; for more details, please see Section S3) and inspected by optical microscopy, atomic force microscopy (AFM), and Raman/PL microspectroscopy. Observation with the optical microscope revealed that the samples had large coverage by $(1L)MoS_2$, and the grains in the continuous areas were found to be triangular in shape. The topographic AFM image of an isolated $(1L)MoS_2$ flake is shown in Figure 1a, and the thickness profile along the (1L) flake is given in Figure 1b. The AFM data revealed that the thickness of the $(1L)MoS_2$ sheet was about 0.7 nm, which is comparable to that reported in the literature.[30]

In the next step, the $TbPc_2$ molecules were characterized by ultraviolet−visible (UV−vis) spectroscopy, Raman spectroscopy, and magnetic measurements (please see Section S1) and deposited onto $(1L)MoS_2$ by thermal evaporation. About half of the sample area was covered before the deposition of $TbPc_2$ in order to obtain a reference area of bare $(1L)MoS_2$ and SiO_2/Si substrate. Figure 1c shows the topography of the $TbPc_2$ layer deposited by thermal vacuum evaporation onto $(1L)MoS_2$. The root-mean-square (rms) roughness was found to be 0.74 nm.

The presence of $TbPc_2$ on $(1L)MoS_2$ after deposition was further confirmed by Raman microspectroscopy, carried out on the $TbPc_2$ and $TbPc_2/(1L)MoS_2$ areas of the sample. The corresponding Raman spectra are presented in Figure 1d. The Raman peaks of the $TbPc_2$ layer are located between 100 and 1600 cm^{-1} and can be attributed to the characteristic bending and stretching vibration modes of the $TbPc_2$, in agreement with the literature (please see Table S1 for selected Raman active modes of $TbPc_2$).[31] For example, peaks located at 677, 730, 1136, and 1336 cm^{-1} correspond to Pc breathing, C−H wagging, pyrrole breathing, and pyrrole stretching, respectively. The Raman spectrum of $TbPc_2/(1L)MoS_2$ was found to be a superposition of individual spectra of $TbPc_2$ and $(1L)MoS_2$, displaying a fluorescence effect in higher wave numbers. The peaks corresponding to the in-plane E' and out-of-plane A_1' Raman modes of $(1L)MoS_2$ were observed at 384 and 402 cm^{-1}, respectively. The most striking differences in the Raman and PL spectra of $(1L)MoS_2$ and $TbPc_2/(1L)MoS_2$ are discussed in more detail later in this section.

As a next step, X-ray photoelectron spectroscopy (XPS) measurements were used to investigate the chemical and electronic properties of $TbPc_2/(1L)MoS_2$. Figure S4a−c shows the core-level spectra for C 1s, N 1s, and Tb $3d_{3/2}$ of $TbPc_2/(1L)MoS_2$ and $TbPc_2$ on Si/SiO_2 substrate. A comparison of spectra from the samples prepared on a different piece of substrates shows negligible energy shifts and small shape variations. This indicates minor interactions between the central Tb atom and the environment. This finding is consistent with a previous study of similar double-decker systems.[32] The Tb $3d_{3/2}$ peak's binding energy at 1276.4 eV (Figure S4b) is also consistent with the previously reported value for $TbPc_2$.[23,32,33] The only discernible difference between the samples can be found in the shape of the N 1s spectra, which were fitted by two components. The low-energy (LE) component at 398.8 eV can be associated with "bulk-like" molecules not in direct contact with the surface, while the high-energy (HE) component at 400.2 eV can be associated with molecules affected by the substrate.[23,34] Figure S4c shows that, for the $TbPc_2/(1L)MoS_2$ sample, LE/HE intensity is lower than that for the $TbPc_2$ sample. This finding is in agreement with the overall lower concentration of $TbPc_2$ species on the surface of the $TbPc_2/(1L)MoS_2$ sample (please see the relative atomic concentration in Table S2). The photoelectron spectrum of Mo 3d recorded for the $TbPc_2/(1L)MoS_2$ sample (Figure S4d) did not reveal any significant change in comparison to the spectra usually obtained from CVD $(1L)MoS_2$ samples. A small amount of molybdenum

https://doi.org/10.1021/acsnano.2c08320
ACS Nano 2023, 17, 2170−2181

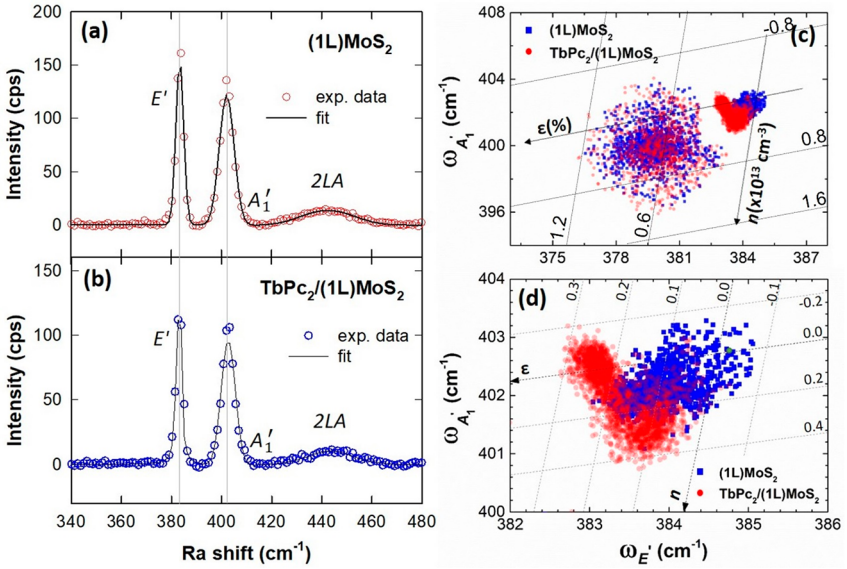

Figure 3. Results of Raman microspectroscopy investigations of $TbPc_2$/(1L)MoS_2. Typical Raman spectra together with the fitted curves shown (a) for (1L)MoS_2 and (b) for $TbPc_2$/(1L)MoS_2. (c) Raman correlation plots: $\omega_{E'}$ vs $\omega_{A_1'}$ for (1L)MoS_2 with and without $TbPc_2$ molecules are shown in the panel. (d) Enlarged portion of the correlation plot (c), showing the axis for doping level (n) and strain (ε), is shown in the panel. The n and ε are estimated as $\times 10^{13}$ cm^{-2} and percentages, respectively.

oxide detected in the spectra is a common residual from CVD growth.

The X-ray reflectivity (XRR) study of $TbPc_2$/(1L)MoS_2 (Figure S5) enabled us to determine the rms, which was found to be 0.56 nm (comparable to the results obtained by AFM). Analysis of the XRR curves yielded the electron density profile, which suggested that the molecules at the layer in the proximity of (1L)MoS_2 tend to orient with the high-symmetry axis perpendicular to the (1L)MoS_2 layer, as has been reported for $TbPc_2$ on graphene,[28] and the degree of order decreases with the distance from the substrate.

Photoluminescence and Raman Microspectroscopy Investigations. The successfully prepared $TbPc_2$/(1L)MoS_2 VSH was further investigated by room-temperature Raman and photoluminescence (PL) microspectroscopy. Figure 2a shows an optical image of a (1L)MoS_2 flake in which approximately the left half of the single crystal is covered with $TbPc_2$ molecules. This region on the edge of the molecular layer was selected to obtain a direct comparative analysis between VSH $TbPc_2$/(1L)MoS_2 and neat (1L)MoS_2 within the same single-crystalline flake. The average PL intensity map plotted on the 610−710 nm scale is shown in Figure 2b. The color code clearly reveals that the $TbPc_2$ molecules induce quenching in the PL spectra of (1L)MoS_2. It can be seen that the average PL intensity is slightly lower in the left portion of the crystal covered with $TbPc_2$ than in the unexposed area. This PL quenching may result from a possible charge transfer at the heterojunction of $TbPc_2$/(1L)MoS_2 before any exciton decay occurs. Similar PL quenching has been reported for other 2D materials decorated with metal phthalocyanines. The effect was rationalized by the value of the redox potential of the molecules, which was situated below the conduction band minima (CBM) of the 2D monolayer.[35] Consequently, it can be suggested that the redox potential of $TbPc_2$ lies below the CBM of (1L)MoS_2 as well. As the PL intensity from the 2D crystal itself is usually nonuniform due to defects and the spatial distribution of doping and strain (as discussed further in the following sections), the quenching also slightly varies across the inspected area. The quenching phenomena can be explained by Q-band absorption of $TbPc_2$; however, charge transfer can occur along with Q-band absorption in such heterostructures.

Representative PL characteristics for the (1L)MoS_2, $TbPc_2$, and $TbPc_2$/(1L)MoS_2 structures are shown in Figure 2d−f, respectively, along with deconvolution of the peaks and a cumulative fit to the overall spectra. The PL of (1L)MoS_2 is characterized by a peak around 670 nm (1.82 eV), which is attributed to the A exciton (ground state exciton) and a shoulder peak around 630 nm (1.95 eV) resulting from the B exciton (coming from the higher energy spin−orbit split state). The ratio of the A and B exciton peak intensities can be considered as a tentative measure of the quality of the single crystalline flake.[12,36] The low intensity of the B exciton peak suggests that (1L)MoS_2 has a relatively small number of defects. The PL spectra from the $TbPc_2$ molecular layer on the SiO_2/Si substrate presented in Figure 2e show a gradual increase in intensity toward lower wavelengths, which can be attributed to excitons resulting from the highest-occupied/lowest-unoccupied molecular orbital (HOMO/LUMO) levels of the $TbPc_2$ molecules.

Finally, Figure 2f displays the PL spectrum of the VSH heterostructure $TbPc_2$/(1L)MoS_2 on the SiO_2/Si substrate along with its deconvolution. The intensity of the defect peak (i.e., B exciton) is elevated due to superposition of the excitons from the molecular layer. Although the PL spectrum of the VSH seems to be roughly a superposition of the individual spectra of (1L)MoS_2 and $TbPc_2$, more detailed analysis revealed that the A exciton peak is moderately red-shifted by 3−5 nm in $TbPc_2$/(1L)MoS_2 in comparison to bare (1L)MoS_2, which suggests a weak interaction between the (1L)MoS_2 and $TbPc_2$ molecules.

To investigate the impact of the $TbPc_2$ molecules on the A and B excitons individually, PL maps of about 30 μm × 30 μm on different 2D single crystals of (1L)MoS_2 with and without

https://doi.org/10.1021/acsnano.2c08320
ACS Nano 2023, 17, 2170−2181

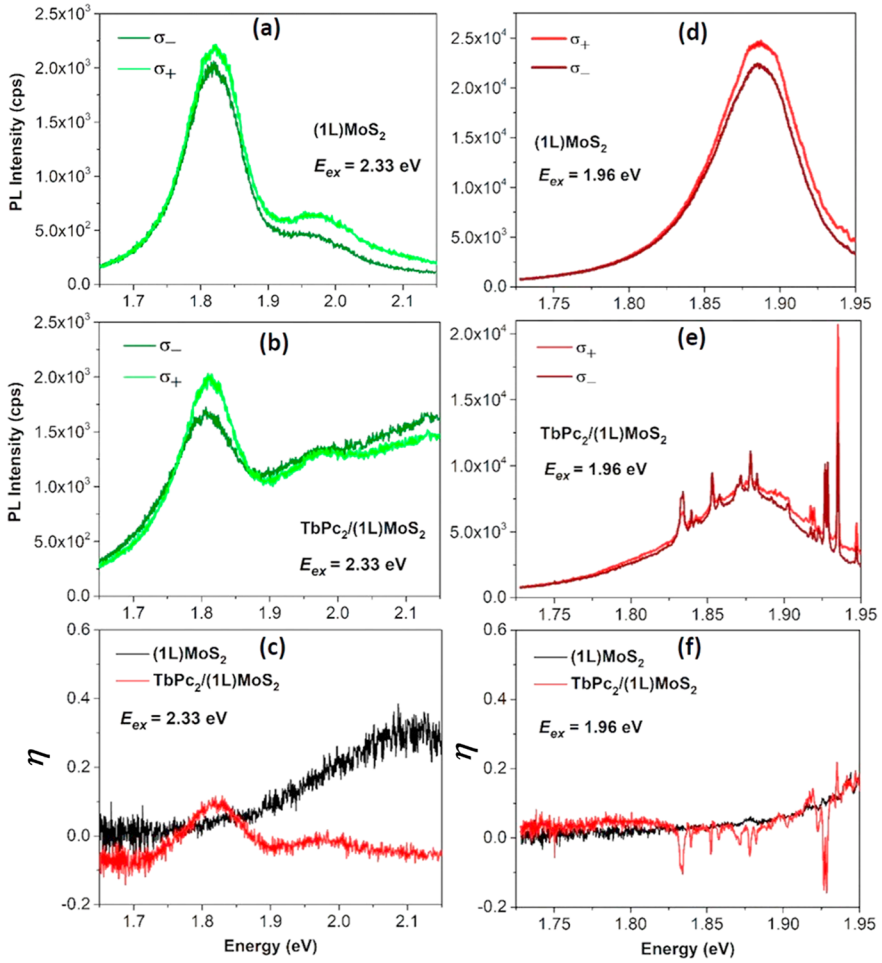

Figure 4. Valley polarization analysis of (1L)MoS_2 and $TbPc_2$/(1L)MoS_2: (a, b) show the excitation of (1L)MoS_2 and $TbPc_2$/(1L)MoS_2, respectively, in off-resonance at E_{ex} = 2.33 eV. (c) The valley polarization (η) as a function of energy estimated from the respective intensities at E_{ex} = 2.33 eV. (d,, e) Show the excitation of (1L)MoS_2 and $TbPc_2$/(1L)MoS_2, respectively, in off-resonance at E_{ex} = 1.96 eV. (f) The valley polarization, η, as a function of energy at E_{ex} = 1.96 eV.

$TbPc_2$ were studied (Figure S6). Typically, the PL spectra of (1L)MoS_2 were dominated by *A* excitons. The PL map of average intensity over the *A* exciton peak in (1L)MoS_2 compared to that of $TbPc_2$/(1L)MoS_2 with the same scale is presented in Figure S6a,b, where overall quenching can be observed.

Interestingly, the average intensity of the *B* exciton peak appears to show a reverse effect, where the presence of $TbPc_2$ molecules on (1L)MoS_2 leads to enhancement of the *B* exciton intensity, as can be seen in Figure S6c,d, respectively. However, this effect can be explained by the contribution of the PL from $TbPc_2$, as there is only a tiny change in the *B* exciton peak due to $TbPc_2$ deposition, as illustrated previously. Figure S6e,f compares the average peak position of the *A* exciton as a function of energy for (1L)MoS_2 and $TbPc_2$/(1L)MoS_2, respectively. The red-shift in $TbPc_2$/(1L)MoS_2 can be observed clearly. The reduction in the PL photon energy of the *A* exciton peak in $TbPc_2$/(1L)MoS_2 (~0.04 eV) suggests a moderate optical band gap change, substantiating the p-doping effect of $TbPc_2$ molecules on (1L)MoS_2, which is corroborated by the Raman spectra analysis discussed below.

Raman spectroscopy is arguably the most common technique for analyzing doping, strain, electron density, and electron−phonon interactions in 2D materials. Typically, charge transfer, doping, and strain phenomena are correlated with the position and width of E' and A_1'peaks in (1L)MoS_2.[37] The most prominent peaks in the Raman spectra of (1L)MoS_2 are located at 384 and 402 cm^{-1} due to in-plane E' and out-of-plane A_1'modes, respectively[18] (Raman spectra extended to the 2LA mode area with negligible changes are shown in Figure S7).

Figure 3a,b shows the comparison between the Raman spectra of pristine (1L)MoS_2 and $TbPc_2$/(1L)MoS_2. The A_1'peak reveals a blue-shift by 3−4 cm^{-1} in $TbPc_2$/(1L)MoS_2 in comparison to the pristine (1L)MoS_2, which is in agreement with the expected p-doping of (1L)MoS_2. Interestingly, the E' peak was marginally red-shifted by 1−2 cm^{-1}, which has been explained as competition between the van der Waals force and dielectric shielding in van der Waals (vdW) heterostructures.[38]

In order to obtain more insight into the influence of $TbPc_2$ molecules on the (1L)MoS_2, a Raman correlation analysis was performed for pristine (1L)MoS_2 and $TbPc_2$/(1L)MoS_2 (Figure S8 shows the Raman shift distribution over the flakes for the E' and A_1'peaks). To extract the information related to the strain and doping effects, a correlation diagram of the Raman shifts of the E' and A_1'modes, which are both influenced by doping and strain, was constructed (Figure 3c,d). The data points for (1L)MoS_2 and $TbPc_2$/(1L)MoS_2 are plotted in blue and red, respectively.

https://doi.org/10.1021/acsnano.2c08320
ACS Nano 2023, 17, 2170−2181

There are two major lobes present in the correlation diagram for each sample area. The first symmetrical lobe around $E' \sim 380\ cm^{-1}$ and $A_1' \sim 400\ cm^{-1}$ is almost identical for both (1L)MoS_2 and $TbPc_2$/(1L)MoS_2. This more diffusive contribution mostly arises from the edges of the flakes. The second lobe is asymmetric; its zoomed version is shown in Figure 3d along with the superimposed iso-strain, ε and iso-doping, and n lines, where the green dot represents the reference for the Raman shift of the pristine-like (mechanically exfoliated) (1L)MoS_2.[39] The defined axis of strain and doping level have been defined previously using Grüneisen parameters of different Raman modes.[39,40] Closer inspection of Figure 3d suggests that the data points of the top right lobe can be further divided into two sublobes with a different slope. The top left lobe has a major contribution from the central region of the flake, while the bottom right lobe corresponds to the edges of the triangular flake. The doping n is moderately increased due to the presence of $TbPc_2$ on (1L)MoS_2, and the values of n are $\sim 0.1 \times 10^{13}\ cm^{-1}$, indicating p-type doping. There is also a slight increase in the strain of about 0.1%, which is more pronounced around the central region of the flake.

To underpin the charge carrier dynamics in (1L)MoS_2 and $TbPc_2$/(1L)MoS_2, time-resolved PL (TRPL) measurements were performed using the fluorescence lifetime imaging (FLIM) technique. The TRPL observations (Figure S11) also corroborate the presence of the photoinduced charge-transfer phenomena discussed above. The appearance of an additional slow decay channel in $TbPc_2$/(1L)MoS_2 is associated with the intersystem charge transfer, which introduces an additional delay, and this is a commonly observed phenomenon in layered heterostructures.[41−43] For more details, please see Section S2.5.

Valley-Selective Emission under CP Light. One of the most striking properties of the TMD monolayers is the strong valley contrast associated with the emission of circularly polarized photons. In order to explore the influence of $TbPc_2$ on the valley-selective emission of (1L)MoS_2, we recorded polarization-resolved PL spectra of as-grown (1L)MoS_2 and $TbPc_2$/(1L)MoS_2 using CP light. We would like to point out that, despite the significant magneto-optical properties of $TbPc_2$, the degree of polarization is not affected by these effects for the given experimental geometry and stacking of the molecules in the layer. The broken spin degeneracy along with time-reversal symmetry define the spin and valleys in (1L)MoS_2, which can be optically excited with the helicity of CP light (left-handed (σ^-) and right-handed (σ^+)) in a selective manner.[44,45] In the first experiment, the PL spectra were recorded under the σ^+ CP laser excitation of energy, E_{ex} = 2.33 eV (off-resonant condition) (see Figure 4a,b). The emission energy dependence of the degree of polarization has been determined as $\eta = (I(\sigma^+) - I(\sigma^-))/(I(\sigma^+) + I(\sigma^-))$, where $I(\sigma^+, \sigma^-)$ are the polarization-resolved PL intensities.

The calculated η dependencies are shown in Figure 4c for the off-resonant case. A significantly lower degree of polarization of the A and B excitons was observed in the as-grown (1L)MoS_2. This is not surprising, as the degree of valley polarization η in (1L)MoS_2 is expected to be negligible at room temperature and in the out-of-resonance condition.[45−47] On the other hand, in the $TbPc_2$/(1L)MoS_2 heterostructure, η was found to be strongly enhanced. This observation is in contrast to the previously observed CP emission from (1L)MoS_2 under off-resonant excitation. Thus, the η enhancement cannot be explained by the intrinsic valley and spin selective response of (1L)MoS_2 to the CP light, and the observed effect must come from the light−matter interaction with the VSH.

We further performed a polarization-resolved experiment under the pumping of close-to-resonance (E_{ex} = 1.96 eV) with B exciton (~1.98 eV). The results are shown in Figure 4d,e for (1L)MoS_2 and $TbPc_2$/(1L)MoS_2, respectively. The corresponding degree of polarization, η, has been shown in Figure 4f. Please note that the PL spectra for the VSH structure are superimposed by the Raman bands of the $TbPc_2$ molecules. A different result, yet consistent with previously observed ones, is obtained: the polarization gradually increases up to ~0.18 in both cases, apart from the "negative Raman glitches" from the $TbPc_2$ molecules in the VSH structure. This observation is consistent with the previous observation of off-resonant excitation due to the fact that the close-to-resonant excitation produces significantly fewer photocarriers in the $TbPc_2$ excited state. Thus, the polarization dependence of (1L)MoS_2 remains independent of $TbPc_2$. The effect persists down to low temperatures and under external magnetic fields (see Figure S10).

Mechanism for Valley-Polarization Enhancement. Prior to entering a deeper discussion of the observed phenomenon, let us briefly summarize the important features of the band structure and related optical transitions of the $TbPc_2$ molecule.[48] In $TbPc_2$, about 2.6 electrons are transferred from the metal to the Pc ligands. The charge transferred from the Tb ion to the ligands is not sufficient to saturate them, as each Pc plane requires two electrons to be saturated. The corresponding unpaired electron has π-character and is delocalized over both ligands. Consequently, the degenerated state occupied by a π-radical is split into a singly occupied molecular orbital (SOMO) state below and LUMO state above the Fermi level with opposite spin indices due to the Pauli Exclusion Principle.[48,49] The $TbPc_2$ reveals two strong $\pi \rightarrow \pi^*$ optical transitions from the SOMO to the LUMO+1 (Q_1) and HOMO to the LUMO (Q_2) orbitals with the absorption maxima located at 1.86 and 2.00 eV, respectively, giving rise to the well-known Q-band.[50]

Moreover, the decoupling between the Tb and ligand spin systems is responsible for the conservation of the electronic properties of the molecule deposited on various substrates. Therefore, we can expect that the main features of the electronic band structure will not be drastically modified due to the interaction with (1L)MoS_2.[48,49,51]

To elucidate the nature of the chemical bond and low-lying excitations of the (1L)MoS_2/$TbPc_2$ interface, we resort to density functional calculations using a hybrid functional PBE0.[52] Figure 5a shows the relaxed geometry, where the Tb atom sits on top of the sulfur. The relaxed distance between the lowest Pc and topmost S layers is ~3.3 Å, typical for physisorption. The Pc planes remain parallel as a result of the vdW attraction.

Figure 5b also shows the density of states (DOS) projected on S, C, and Tb atoms. The S contribution to the DOS indicates the edges of the valence and conduction bands. We see that the gap size does not change due to adsorption (up to few percent) by comparing to the DOS of pristine MoS_2. The DOS of the molecular species is devoid of any Tb contribution within the bulk gap. The DOS of C shows four in-gap peaks occupied by three electrons, i.e., carrying spin-half moment. This is the ligand spin, known from $TbPc_2$ in isolation. Thus, the overall charge transfer to the molecule is moderate and

https://doi.org/10.1021/acsnano.2c08320
ACS Nano 2023, 17, 2170−2181

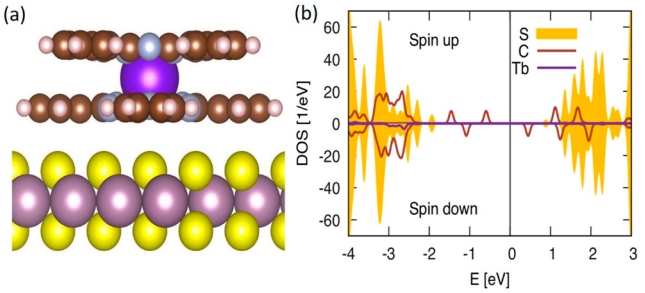

Figure 5. (a) Ball-and-stick model of the relaxed $TbPc_2/MoS_2$ structure (S = yellow, Mo = violet, C = brown, H = pink, N = gray, and Tb = magenta). (b) Density of states projected on the S, C, and Tb atoms for both spin directions from the density functional theory (DFT) calculation. The zero energy separates the occupied and unoccupied states. An artificial Gaussian broadening of the resonances is applied.

orbital unspecific. Consequently, we conclude that the electronic structure of the adsorbed molecule is only slightly perturbed compared to the molecule in isolation. Thus, the major mechanism behind the chiral light emission is originated from the valley-related excitons in $(1L)MoS_2$.

In order to understand the inequity in the optical intensities for the emission upon the irradiation with the circularly polarized light, we use the pseudospin formalism to explore the dynamics of the bright exciton doublet in the $MoS_2/TbPc_2$ heterostructure. The approach considers competing relaxation mechanics from exciton exchange and from single-particle spin flip into optically inactive states. In this approach, the 2×2 density matrix $\rho_{\mathbf{q}}$ of MoS_2 excitons with center-of-mass momentum $\mathbf{q} = (q \cos\phi, q \sin\phi, 0)$ is presented in the form:

$$\rho_{\mathbf{q}} = n_{\mathbf{q}}\mathcal{J} + \mathbf{S}_{\mathbf{q}} \cdot \boldsymbol{\sigma}. \tag{1}$$

Here, $n_{\mathbf{q}} = \mathrm{Tr}[\rho_{\mathbf{q}}]/2$, the pseudospin-average-distribution function of the excitons, $\mathcal{J}$ is the 2×2 unity matrix, $(\mathbf{S}_{\mathbf{q}})_j = \mathrm{Tr}[\rho_{\mathbf{q}}\sigma_j]/2$, where $j = x, y$, and z are components of the pseudospin, σ_j is the Pauli matrix, and "." is the state for the scalar product. The S_z component describes the valley polarization, while the S_x and S_y components define the valley coherences of the excitons in the monolayer. The pseudospins satisfy the Maialle-Silva-Sham (SMM) equation:[53]

$$\frac{\partial \mathbf{S}_{\mathbf{q}}}{\partial t} = \boldsymbol{\Omega}_{\mathbf{q}} \times \mathbf{S}_{\mathbf{q}} + \sum_{\mathbf{q}\mathbf{q}'} W_{\mathbf{q}\mathbf{q}'}[\mathbf{S}_{\mathbf{q}'} - \mathbf{S}_{\mathbf{q}}] - \frac{\mathbf{S}_{\mathbf{q}}}{\tau} + \mathbf{G} \tag{2}$$

The term $\boldsymbol{\Omega}_{\mathbf{q}} = (\Omega_{\parallel} \cos(2\varphi), \Omega_{\parallel} \sin(2\varphi), 0)$ represents the effective pseudospin precession frequency. It is originated from the long-range exchange interaction between the exciton states of different valleys (see details in ref 54). $W_{\mathbf{q}\mathbf{q}'}$ is the scattering rate induced by the impurities, exciton−phonon interaction, and exciton−exciton interaction, τ represents the decay time of the excitons, and $\mathbf{G}$ describes the external source of the valley coherence (G_x, G_y) and valley polarization (G_z) in the system."×" stands for the vector product. Solving the MSS equation for $G_z \neq 0$, $G_x = G_y = 0$, one can observe that the steady-state valley polarization $\eta \propto S_z$ is suppressed by Ω even in the absence of the scattering $W_{\mathbf{q}\mathbf{q}'} = 0$:

$$S_z = \frac{G_z\tau}{1 + \Omega_{\parallel}^2\tau^2} \tag{3}$$

This expression also demonstrates the decreasing of the valley coherence with the larger decay time τ. Since the parameter τ contains the contribution from the radiative decay as well as from nonradiative processes, its value can be dependent on the details of the experiment and the studied samples.

For example, the effective exciton decay time in TMDs can depend on temperature.[55] Namely, at the low-temperature limit, the thermalized excitons are localized at the radiative zone $q < q_{\mathrm{rad}} = \omega_{\mathrm{ex}}/c$ according to the Boltzmann distribution. Here, ω_{ex} is the minimal frequency of light, which causes bright exciton transitions. Such excitons mainly decay radiatively with τ_{rad} of a few picoseconds. At high temperatures, the situation is changed, because a part of the exciton population is localized outside of the radiative region and forms the nonradiative reservoir. To depopulate this reservoir, the excitons from nonradiative states must be relaxed to the radiative region. Such a relaxation process includes the exciton−phonon interaction and takes much longer time τ_{eff}, up to nanoseconds.[56] This time can be effectively incorporated in the MSS equation by replacing the second and third terms in eq 2 by $-\mathbf{S}_{\mathbf{q}}/\tau_{\mathrm{eff}}$. Therefore, for this case, one can estimate the strong decrease of the valley polarization by replacing τ with τ_{eff} in eq 3.

In the experiments with the $(1L)MoS_2/TbPc_2$ heterostructure, the parameters $\Omega_{\mathbf{q}}$ and $W_{\mathbf{q}\mathbf{q}'}$ cannot depend on the frequency of the incident light. Hence, we conclude that the observed difference in valley polarizations of $(1L)MoS_2/TbPc_2$ can appear only from the effective relaxation times.

Let us consider two experimental cases and analyze the possible modification of the relaxation times in each case. In the first case, the heterostructure is shined upon by the light of the energy $E = 2.33$ eV. This energy is much larger than the energy of the Q_1 ($E_{Q1} = 1.86$ eV) and Q_2 ($E_{Q2} = 2$ eV) transitions in the $TbPc_2$ molecule. Hence, this component remains unexcited, and all the light energy is transferred to the monolayer and generates the so-called hot excitons. These excitons lose their energy due to exciton−phonon and other many-body interactions and reach, in particular, the lowest energies of A ($E_A = 1.78$ eV) and B ($E_B = 1.98$ eV) transitions in the studied heterostructure. Both transitions are clearly visible.

Moreover, the A exciton line demonstrates the nonzero valley polarization $\eta \approx 20\%$. The experiment is done at room temperature $T = 300$ K, and one can assume that phonons of MoS_2 are in thermodynamic equilibrium. However, these phonons cannot affect the phonons in $TbPc_2$, since the vibrational modes of both layers are not coupled, as confirmed by Raman spectroscopy (see Figure 1d). Hence, the molecules cannot be excited and equilibrated by the phonons of MoS_2. The only way to excite the molecular layer is the Coulomb-induced near-resonant energy transfer between excitons of the MoS_2 and $TbPc_2$ layers. This special process modifies the dynamics of the excitons in the considered system.

Considering that excitons can emit or absorb phonons with average energy $E_{\mathrm{ph}}(T)$ at temperature T, we conclude that excitons in the energy domain $\Delta E \in [E_{Q1} - E_{\mathrm{ph}}(T), E_{Q1} + E_{\mathrm{ph}}(T)]$ nonradiatively decay by transferring their energy to the molecules. The average phonon energy can be estimated as $E_{\mathrm{ph}}(T) \approx k_B T = 26$ meV. Since $E_{Q1} - E_{\mathrm{ph}}(T) - E_A \approx 54$ meV $\gg (\hbar q_{\mathrm{rad}})^2/2m_{\mathrm{ex}} \approx 3$ μeV (m_{ex} is the exciton mass), the excitons in the radiative region are not affected by such process. In other words, the molecular layer works as an

https://doi.org/10.1021/acsnano.2c08320
ACS Nano 2023, 17, 2170−2181

"energy drain" for the nonradiative excitonic states giving rise to a mechanism schematically visualized in Figure 6.

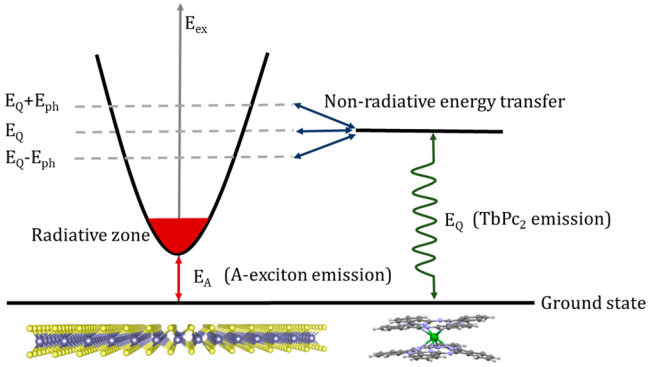

Figure 6. Schematic illustration of the nonradiative energy drain mechanism. The scheme shows the nonradiative energy transfer between the TMD component (left) and $TbPc_2$ molecular magnet (right) together with the essential radiative optical processes in both components of the VSH.

The drained energy excites the $TbPc_2$ molecules, which re-emit photons of broad energy range which, however, does not overlap with the energy of the *A* exciton. Therefore, these photons do not give a contribution to the valley polarization of the *A* exciton. The TRPL analysis presented in Figure S11 supports these findings. This emission explains naturally the similarity of the TRPL decay profiles for $MoS_2/TbPc_2$ and $TbPc_2$ layers, presented in Figure S11e,f, respectively. Since the reservoir of nonradiative excitons is depleted by the energy drain process, none of them scatter into the radiative region and increase the effective lifetime of the excitons in the radiative zone. It results to the nonzero valley polarization in the *A* exciton emission. A similar effect of long-lived exciton filtering was considered earlier for the case of the graphene/TMD heterostructures.[57]

Finally, similar arguments cannot be applied to the *B* excitons, since $E_{Q2} - E_B = 20$ meV is comparable with the phonon energy $E_{ph} \approx 26$ meV. In this case, the energy transfer between the radiative zone of the *B* excitons and $TbPc_2$ molecules is possible and the dynamics of the non- and radiative excitons remain coupled.

In the second type of experiment, the studied heterostructure is shined by the light of energy $E = 1.96$ eV. This energy is close to the energy of the Q_2 transition, and the molecular layer can be excited in this case. Due to relaxation processes in the magnetic molecules, the lowest energy Q_1 type transitions are also activated, leaving no room for energy transfer from the excitons of the monolayer. Therefore, the aforementioned energy drain is blocked in such a case, and the excitons experience dynamics as in the regular monolayer at temperature $T = 300$ K. Such dynamics leads to near-zero valley polarization $\eta \approx 0$ at $T = 300$ K due to a large effective exciton decay time.

CONCLUSIONS AND OUTLOOK

In conclusion, we propose a class of layered hybrid materials composed of 2D semiconductors and single-molecule magnets with intrinsic diverse spin (valley) degrees of freedom. The prototype VSH was successfully prepared by thermal evaporation of $TbPc_2$ molecules on $(1L)MoS_2$ grown by a one-step CVD process on the SiO_2/Si substrate. The persistence of the $TbPc_2$ molecules after deposition was unambiguously confirmed using both microscopic and spectroscopic techniques (AFM, Raman and PL microspectroscopy, XRR, and XPS). The interaction of $TbPc_2$ and $(1L)MoS_2$ spin components was explored using Raman and PL microspectroscopy. We clearly observed that the PL signal is moderately quenched in the VSH compared to the pristine $(1L)MoS_2$, which is attributed to a superficial charge transfer between $TbPc_2$ and $(1L)MoS_2$. Correspondingly, a moderate red-shift observed for the *A* exciton implies an optical bandgap in $TbPc_2/(1L)MoS_2$ changes. TRPL and Raman spectroscopy results also point to the presence of p-type doping due to photogenerated electron transfer between the $TbPc_2$ molecule and $(1L)MoS_2$.

Nevertheless, the most striking observation is that the interaction of the $TbPc_2$ molecules with $(1L)MoS_2$ enhances the polarization of the *A* exciton-related valley, despite an off-resonance condition and room temperature. To explain this unanticipated effect, we propose a nonradiative energy drain mechanism in which the population of the nonradiative excitons is depleted via interaction with the unoccupied electronic states of the molecular magnet. This process partly blocks the scattering of the nonradiative excitons in the radiative region and does not increase the effective lifetime of the excitons in the radiative zone, giving rise to the nonzero valley polarization in the *A* exciton-related emission.

Thanks to the fascinating properties, feasible production, and great stability, the layered hybrid materials composed of monolayer TMDs and double-decker molecule magnets represent multiresponsive and multioperable opto-spin-valletronic platforms capable of chiral light emission, exploitable in the emerging proposals for information storage and quantum computing.

METHODS

Growth of $(1L)MoS_2$. $(1L)MoS_2$ was synthesized on SiO_2/Si substrate using the one-step CVD method in a horizontal single-zone furnace at atmospheric pressure. Details of this process and the experimental setup are provided in Section S3. The morphology and size of the $(1L)MoS_2$ monolayers were characterized by an optical microscope. The thickness of $(1L)MoS_2$ was found to be ~0.7 nm using AFM profilometry.

Preparation of $TbPc_2$. The $[TbPc_2]^0$ complex was synthesized according to the published procedure.[58] A mixture of 1,2-dicyanobenzene (15.6 mmol), $Tb(acac)_3{\cdot}4H_2O$ (1.9 mmol), and DBU (7.8 mmol) in 20 mL of pentan-1-ol was refluxed for 2 days. The solution was allowed to cool down to room temperature; 1.5 mL of acetic acid was added, and the mixture was heated at 100 °C for 0.5 h. After cooling, the precipitate was collected by filtration and washed with *n*-hexane and Et_2O. The crude product was dissolved in 300 mL of the $CHCl_3$/MeOH mixture (1:1, v/v), and PcH_2 was filtered off as a purple solid. The reaction mixture was then left overnight, adsorbed on active basic alumina oxide, and purified by column chromatography on basic alumina oxide deactivated with 4.6% of H_2O (level IV) with $CHCl_3$/MeOH (10:1, v/v) as an eluent. After an additional purification by column chromatography on silica gel ($CHCl_3$/MeOH, 10:1, v/v), the $[TbPc_2]^0$ complex, as a dark green solid, was precipitated from the $CHCl_3$/*n*-hexane mixture, filtered off, and dried in a vacuum. The neutral state of the complex was confirmed by UV–vis spectroscopy (presented in Figure S1). The pristine powder of $TbPc_2$ was also characterized with Raman spectroscopy (Figure S2) and magnetic measurements (Figure S3).

Preparation of $TbPc_2/(1L)MoS_2$ VSH. The SiO_2/Si substrate with $(1L)MoS_2$ was taken to an organic evaporator, and a thin layer with a nominal thickness of ~9 nm of $TbPc_2$ was subsequently evaporated at 400 °C onto the $(1L)MoS_2$ at $\sim 10^{-6}$ mbar of pressure

https://doi.org/10.1021/acsnano.2c08320
ACS Nano 2023, 17, 2170–2181

to obtain a $TbPc_2/(1L)MoS_2$ heterostructure. A reference sample of $TbPc_2$ on SiO_2/Si substrate was obtained using the same protocol. The ∼9 nm thickness of the $TbPc_2$ thin film and the orientational order of the molecules in the $TbPc_2$ layer were further confirmed with XRR. The presence of $TbPc_2$ was also confirmed by XPS and Raman spectroscopy.

Characterization Methods. AFM images and thickness profiles of the structures were acquired using Bruker's AFM Dimension ICON system in the quantitative nonmechanical mode. A Bruker silicon tip was used to acquire AFM data, and Gwyddion software was used to process and analyze the AFM images.

In the XRR experiment, specular X-ray reflection was measured on a rotating-anode X-ray diffractometer RIGAKU Smartlab (45 kV, 200 mA) using Cu Kα radiation and a parabolic multilayer mirror on the primary side; the angular resolution of the whole experimental setup was 0.005°. The reflection curves were fitted to a three-layer model. For each layer, we determined its thickness (T_n), root-mean square (rms) roughness σ_n, and the electron density ρ_n relative to the fixed electron density of the Si substrate, ρ_{Si}. For the fitting procedure, we used standard reflectivity software based on the Nevot-Croce and Parrat formulas.[59]

Magnetization measurements were performed with a Physical Property Measurement System equipped with a vibrating sample magnetometer (VSM) (Quantum Design) in the temperature range of 2−300 K with an applied magnetic field up to 14 T. The powder sample (mass ∼ 2 mg) was placed in an original Quantum Design sample holder for VSM and pressed carefully to minimize movement of the powder particles during the experiments.

For UV−vis characterization, a UV−vis-NIR PerkinElmer Lambda 1050 spectrometer was used. The samples were dissolved in chloroform and measured in quartz cuvettes.

The XPS measurements were performed using a VG ESCA3MkII electron spectrometer with a base pressure over 10^{-9} mbar. Al Kα radiation was used for the excitation of the electrons. The electrons were energy analyzed using a hemispherical analyzer operating at a constant pass energy of 20 eV. The estimated error in binding energy determination was ±0.1 eV. The spectra were calibrated by setting the C 1s peak belonging to hydrocarbon and/or adventitious carbon at the binding energy of 285 eV. The Mo 3d, C 1s, N 1s, and Tb $3d_{3/2}$ photoelectrons were measured. The Tb $3d_{3/2}$ line is the only one usable to confirm the presence of Tb due to the overlap of the Tb 4d line with Si 2s and the overlap of the $3d_{5/2}$ line with the KVV Auger peak of carbon. The spectra were curve-fitted using the Gaussian−Lorentzian line shape after subtraction of the Shirley background. The surface atomic content was accomplished assuming a homogeneous distribution of atoms, Wagner sensitivity factors, and corrections for the analyzer transmission function.

Optical Microspectroscopies. Raman and PL spectra of both pristine $(1L)MoS_2$ and $TbPc_2/(1L)MoS_2$ were collected in the backscattering geometry with an excitation wavelength of 532 nm (2.33 eV) at 200 μW power using a WITec spectrometer at room temperature. Flakes with a scale size of about 30 μm were selected and mapped for PL and Raman spectra with a spatial resolution of 0.5 μm using a grating of 600 and 1800 lines/mm, respectively.

CP-PL and Raman measurements were carried out in LabRAM HR Evolution (Horiba) by exciting the samples with σ^+ helicity. The CP Raman spectra for $TbPc_2/(1L)MoS_2$ were obtained using an incident excitation of 532 nm (2.33 eV), while CP-PL was carried out with energy excitations of both 633 nm (1.96 eV) and 532 nm (2.33 eV). A $\lambda/4$ plate was placed just before the objective, and the incoming orientation was chosen using a $\lambda/2$ plate, whereas the outgoing orientation was selected using a polarizer. The helicity of the light impacting the sample was optimized using a Thorlabs TXP 5004 polarimeter, whereas the helicity of the scattered light was optimized by searching for the minimum (or maximum) intensity of the Rayleigh line reflected from a thick, sputtered Au film. It is well-known that the performance of a charge coupled device (CCD) is strongly dependent on the helicity of the incoming light. In order to avoid these polarization sensitivities of the CCD, we put a depolarizer in front of the detector. The CP-PL and CP Raman spectra were obtained using 150 and 1800 lines/mm gratings, respectively.

The temperature-dependent Raman and PL spectra were measured in the backscattering geometry using a low-temperature confocal Raman microscope insert (attoRAMAN, attocube) placed in a Physical Property Measurement System (PPMS, Quantum Design). A low temperature and magnetic field compatible 100× objective (numerical aperture 0.82 and lateral resolution of 500 nm) lens were used to focus the 632.8 nm HeNe laser beam of pump fluence ∼ 250 μW. The low-frequency Raman spectra were obtained down to ±10 cm^{-1} by combining two volume Bragg grating notch filters into the Raman system to suppress the Rayleigh signal. The incident laser beam was circularly polarized using a set of standard 633 nm half and quarter-wave plates. Similarly, a series of broadband quarter and half-wave plates have been used to obtain polarization-resolved emitted signals. The degree of polarization was precalibrated for each incident and scattered beam (ellipticity > 44.5°) using ThorLabs's TXP polarimeter. The spectral resolution of the spectrometer under the measurement condition using 1800 lines/cm grating was 0.6 cm^{-1}. The intensity response of the CCD detector was precalibrated using a tungsten halogen light source (HL-2000-CAL, Ocean Optics). The spectra integration times were 120 s to achieve good signals. Apart from the PPMS temperature readout, the actual temperature of the sample was monitored through a thermometer mounted on the optical insert at the sample position, and the spectra were recorded while the temperature stabilized at the measured point during the cooling cycle from 3000 to 10K K.

TRPL measurements were recorded with an Olympus Fluo-View1000 confocal system coupled to a PMT detector (tau-SPAD, Picoquant) with subnanosecond time correlated single photon counting (TCSPC) capability (HydraHarp 400, Picoquant). A long-pass filter (edge at 580 nm) was used to record the lifetimes of both the structures. The samples were excited with a 532 nm laser (2.33 eV; LDH-P-FA Series, Picoquant) with a power of 6.5 nW μm^2, a frequency of 40 MHz, and a pulse duration of 80 ps. Consequently, FLIM was also performed, and the lifetime maps were acquired. The decay profiles were fitted with a single-exponential decay function.

DFT Calculations. Kohn−Sham states were represented using a localized basis set, as implemented in the FHI-AIMS package.[60] Relativistic corrections were included at the scalar level in the atomic zero order regular approximation.[60] To account for exchange correlation, we employed the PBE functional[61] for the geometry relaxation and PBE0 functional[52] for calculating the density of states. We checked our results against the B3LYP functional[62] and did not find qualitative changes. All calculations included the C_6/R^6 van der Waals contribution to the forces from the Tkatchenko−Scheffler partitioning.[63] We used the BFGS algorithm for relaxation, until the absolute value of the maximum force component dropped below 0.01 eV/Å. We started the structural relaxations with the molecule situated in diverse lateral positions (on-S, on-Mo, hollow) and diverse angles relative to the crystalline directions. The result was always a physisorption, as depicted in the main text. We estimated the charge transfer to the molecule using the Mulliken technique, yielding less than 2% electrons.

ASSOCIATED CONTENT

Supporting Information

The Supporting Information is available free of charge at https://pubs.acs.org/doi/10.1021/acsnano.2c08320.

Additional results related to the synthesis and characterization of $TbPc_2$, MoS_2, and $TbPc_2/(1L)MoS_2$; optical and magnetic characterization of $TbPc_2$; XPS and X-ray reflectivity data of $TbPc_2/(1L)MoS_2$ along with additional Raman/PL/valley polarization (with E_X = 2.33 eV) analysis and time-resolved PL data; CVD growth of MoS_2 (PDF)

https://doi.org/10.1021/acsnano.2c08320
ACS Nano 2023, 17, 2170−2181

AUTHOR INFORMATION

Corresponding Authors

Jana Vejpravova − *Department of Condensed Matter Physics, Faculty of Mathematics and Physics, Charles University, 121 16 Prague 2, Czech Republic;* orcid.org/0000-0002-6308-9992; Email: jana@mag.mff.cuni.cz

Martin Kalbac − *J. Heyrovsky Institute of Physical Chemistry, 182 23 Prague 8, Czech Republic;* orcid.org/0000-0001-9574-4368; Email: martin.kalbac@jh-inst.cas.cz

Authors

Vaibhav Varade − *Department of Condensed Matter Physics, Faculty of Mathematics and Physics, Charles University, 121 16 Prague 2, Czech Republic*

Golam Haider − *J. Heyrovsky Institute of Physical Chemistry, 182 23 Prague 8, Czech Republic;* orcid.org/0000-0001-5300-3764

Artur Slobodeniuk − *Department of Condensed Matter Physics, Faculty of Mathematics and Physics, Charles University, 121 16 Prague 2, Czech Republic*

Richard Korytar − *Department of Condensed Matter Physics, Faculty of Mathematics and Physics, Charles University, 121 16 Prague 2, Czech Republic;* orcid.org/0000-0003-4949-4147

Tomas Novotny − *Department of Condensed Matter Physics, Faculty of Mathematics and Physics, Charles University, 121 16 Prague 2, Czech Republic;* orcid.org/0000-0001-7014-4155

Vaclav Holy − *Department of Condensed Matter Physics, Faculty of Mathematics and Physics, Charles University, 121 16 Prague 2, Czech Republic*

Jiri Miksatko − *J. Heyrovsky Institute of Physical Chemistry, 182 23 Prague 8, Czech Republic*

Jan Plsek − *J. Heyrovsky Institute of Physical Chemistry, 182 23 Prague 8, Czech Republic*

Jan Sykora − *J. Heyrovsky Institute of Physical Chemistry, 182 23 Prague 8, Czech Republic;* orcid.org/0000-0003-0936-9368

Miriam Basova − *Department of Condensed Matter Physics, Faculty of Mathematics and Physics, Charles University, 121 16 Prague 2, Czech Republic*

Martin Zacek − *Department of Condensed Matter Physics, Faculty of Mathematics and Physics, Charles University, 121 16 Prague 2, Czech Republic*

Martin Hof − *J. Heyrovsky Institute of Physical Chemistry, 182 23 Prague 8, Czech Republic*

Complete contact information is available at: https://pubs.acs.org/10.1021/acsnano.2c08320

Notes

The authors declare no competing financial interest.

ACKNOWLEDGMENTS

This research was funded by the European Research Council (project no. 716265). The authors acknowledge the assistance provided by the Research Infrastructures MGML (Project No. LM2018096) and NanoEnviCz (Project No. LM2015073), supported by the Ministry of Education, Youth and Sports of the Czech Republic. R.K. acknowledges the Czech Science foundation (project no. 22-22419S). G.H., J.M., J.P. and M.K. acknowledge Czech Science foundation Expro project No. 20-08633X, and J.S., M.H. acknowledge Czech Science foundation Expro project No. 19-26854X. The authors acknowledge Dr. T. Verhagen for his support in low-temperature Raman/PL measurements and TRPL data analysis and Dr. V. Guerra for his kind assistance in the UV−vis experiments.

REFERENCES

(1) Allen, M. J.; Tung, V. C.; Kaner, R. B. Honeycomb Carbon: A Review of Graphene. *Chem. Rev.* **2010**, *110*, 132−145.

(2) Xu, M.; Liang, T.; Shi, M.; Chen, H. Graphene-like Two-Dimensional Materials. *Chem. Rev.* **2013**, *113* (5), 3766−3798.

(3) Fiori, G.; Bonaccorso, F.; Iannaccone, G.; Palacios, T.; Neumaier, D.; Seabaugh, A.; Banerjee, S. K.; Colombo, L. Electronics Based on Two-Dimensional Materials. *Nat. Nanotechnol.* **2014**, *9* (10), 768−779.

(4) Eda, G.; Maier, S. A. Two-Dimensional Crystals: Managing Light for Optoelectronics. *ACS Nano* **2013**, *7* (7), 5660−5665.

(5) Butler, S. Z.; Hollen, S. M.; Cao, L.; Cui, Y.; Gupta, J. A.; Gutiérrez, H. R.; Heinz, T. F.; Hong, S. S.; Huang, J.; Ismach, A. F.; Johnston-Halperin, E.; Kuno, M.; Plashnitsa, V. v.; Robinson, R. D.; Ruoff, R. S.; Salahuddin, S.; Shan, J.; Shi, L.; Spencer, M. G.; Terrones, M.; Windl, W.; Goldberger, J. E. Progress, Challenges, and Opportunities in Two-Dimensional Materials beyond Graphene. *ACS Nano* **2013**, *7* (4), 2898−2926.

(6) Radisavljevic, B.; Whitwick, M. B.; Kis, A. Integrated Circuits and Logic Operations Based on Single-Layer MoS 2. *ACS Nano* **2011**, *5* (12), 9934−9938.

(7) Wang, G.; Chernikov, A.; Glazov, M. M.; Heinz, T. F.; Marie, X.; Amand, T.; Urbaszek, B. Colloquium: Excitons in Atomically Thin Transition Metal Dichalcogenides. *Rev. Mod. Phys.* **2018**, *90* (2), 021001.

(8) Onga, M.; Zhang, Y.; Ideue, T.; Iwasa, Y. Exciton Hall Effect in Monolayer MoS 2. *Nat. Mater.* **2017**, *16* (12), 1193−1197.

(9) Splendiani, A.; Sun, L.; Zhang, Y.; Li, T.; Kim, J.; Chim, C. Y.; Galli, G.; Wang, F. Emerging Photoluminescence in Monolayer MoS2. *Nano Lett.* **2010**, *10* (4), 1271−1275.

(10) Mouri, S.; Miyauchi, Y.; Matsuda, K. Tunable Photoluminescence of Monolayer MoS2 via Chemical Doping. *Nano Lett.* **2013**, *13*, 5944−5948.

(11) Chow, P. K.; Jacobs-Gedrim, R. B.; Gao, J.; Lu, T. M.; Yu, B.; Terrones, H.; Koratkar, N. Defect-Induced Photoluminescence in Monolayer Semiconducting Transition Metal Dichalcogenides. *ACS Nano* **2015**, *9* (2), 1520−1527.

(12) Verhagen, T.; Guerra, V. L. P.; Haider, G.; Kalbac, M.; Vejpravova, J. Towards the Evaluation of Defects in MoS2 Using Cryogenic Photoluminescence Spectroscopy. *Nanoscale* **2020**, *12* (5), 3019−3028.

(13) Habib, M. R.; Li, H.; Kong, Y.; Liang, T.; Obaidulla, S. M.; Xie, S.; Wang, S.; Ma, X.; Su, H.; Xu, M. Tunable Photoluminescence in a van Der Waals Heterojunction Built from a MoS2Monolayer and a PTCDA Organic Semiconductor. *Nanoscale* **2018**, *10* (34), 16107−16115.

(14) Choudhury, P.; Ravavarapu, L.; Dekle, R.; Chowdhury, S. Modulating Electronic and Optical Properties of Monolayer MoS2 Using Nonbonded Phthalocyanine Molecules. *J. Phys. Chem. C* **2017**, *121* (5), 2959−2967.

(15) Tohgha, U.; Deol, K. K.; Porter, A. G.; Bartko, S. G.; Choi, J. K.; Leonard, B. M.; Varga, K.; Kubelka, J.; Muller, G.; Balaz, M. Ligand Induced Circular Dichroism and Circularly Polarized Luminescence in Cdse Quantum Dots. *ACS Nano* **2013**, *7* (12), 11094−11102.

(16) Amsterdam, S. H.; Stanev, T. K.; Zhou, Q.; Lou, A. J. T.; Bergeron, H.; Darancet, P.; Hersam, M. C.; Stern, N. P.; Marks, T. J. Electronic Coupling in Metallophthalocyanine-Transition Metal Dichalcogenide Mixed-Dimensional Heterojunctions. *ACS Nano* **2019**, *13* (4), 4183−4190.

(17) Haldar, S.; Bhandary, S.; Vovusha, H.; Sanyal, B. Comparative Study of Electronic and Magnetic Properties of Iron and Cobalt

Phthalocyanine Molecules Physisorbed on Two-Dimensional MoS2 and Graphene. *Phys. Rev. B* **2018**, *98* (8), 854401.
(18) Ghimire, G.; Adhikari, S.; Jo, S. G.; Kim, H.; Jiang, J.; Joo, J.; Kim, J. Local Enhancement of Exciton Emission of Monolayer MoS2 by Copper Phthalocyanine Nanoparticles. *J. Phys. Chem. C* **2018**, *122* (12), 6794−6800.
(19) Padgaonkar, S.; Amsterdam, S. H.; Bergeron, H.; Su, K.; Marks, T. J.; Hersam, M. C.; Weiss, E. A. Molecular-Orientation-Dependent Interfacial Charge Transfer in Phthalocyanine/MoS2Mixed-Dimensional Heterojunctions. *J. Phys. Chem. C* **2019**, *123* (21), 13337−13343.
(20) Kafle, T. R.; Kattel, B.; Lane, S. D.; Wang, T.; Zhao, H.; Chan, W. L. Charge Transfer Exciton and Spin Flipping at Organic-Transition-Metal Dichalcogenide Interfaces. *ACS Nano* **2017**, *11* (10), 10184−10192.
(21) Xu, R.; Xuan, F.; Quek, S. Y. Spin-Dependent Tunneling Barriers in CoPc/VSe2from Many-Body Interactions. *J. Phys. Chem. Lett.* **2020**, *11* (21), 9358−9363.
(22) Branzoli, F.; Carretta, P.; Filibian, M.; Zoppellaro, G.; Graf, M. J.; Galan-Mascaros, J. R.; Fuhr, O.; Brink, S.; Ruben, M. Spin Dynamics in the Negatively Charged Terbium (III) Bis-Phthalocyaninato Complex. *J. Am. Chem. Soc.* **2009**, *131* (22), 7934−7934.
(23) Mannini, M.; Bertani, F.; Tudisco, C.; Malavolti, L.; Poggini, L.; Misztal, K.; Menozzi, D.; Motta, A.; Otero, E.; Ohresser, P.; Sainctavit, P.; Condorelli, G. G.; Dalcanale, E.; Sessoli, R. Magnetic Behaviour of TbPc 2 Single-Molecule Magnets Chemically Grafted on Silicon Surface. *Nature Comm.* **2014**, *5*, 1−8.
(24) Lodi Rizzini, A.; Krull, C.; Balashov, T.; Kavich, J. J.; Mugarza, A.; Miedema, P. S.; Thakur, P. K.; Sessi, V.; Klyatskaya, S.; Ruben, M.; Stepanow, S.; Gambardella, P. Coupling Single Molecule Magnets to Ferromagnetic Substrates. *Phys. Rev. Lett.* **2011**, *107* (17), 1−5.
(25) Lodi Rizzini, A.; Krull, C.; Balashov, T.; Mugarza, A.; Nistor, C.; Yakhou, F.; Sessi, V.; Klyatskaya, S.; Ruben, M.; Stepanow, S.; Gambardella, P. Exchange Biasing Single Molecule Magnets: Coupling of TbPc2 to Antiferromagnetic Layers. *Nano Lett.* **2012**, *12* (11), 5703−5707.
(26) Moreno Pineda, E.; Komeda, T.; Katoh, K.; Yamashita, M.; Ruben, M. Surface Confinement of TbPc2-SMMs: Structural, Electronic and Magnetic Properties. *Dal. Trans.* **2016**, *45* (46), 18417−18433.
(27) Krainov, I. v.; Klier, J.; Dmitriev, A. P.; Klyatskaya, S.; Ruben, M.; Wernsdorfer, W.; Gornyi, I. v. Giant Magnetoresistance in Carbon Nanotubes with Single-Molecule Magnets TbPc2. *ACS Nano* **2017**, *11* (7), 6868−6880.
(28) Lopes, M.; Candini, A.; Urdampilleta, M.; Reserbat-Plantey, A.; Bellini, V.; Klyatskaya, S.; Marty, L.; Ruben, M.; Affronte, M.; Wernsdorfer, W.; Bendiab, N. Surface-Enhanced Raman Signal for Terbium Single-Molecule Magnets Grafted on Graphene. *ACS Nano* **2010**, *4* (12), 7531−7537.
(29) Serrano, G.; Velez-Fort, E.; Cimatti, I.; Cortigiani, B.; Malavolti, L.; Betto, D.; Ouerghi, A.; Brookes, N. B.; Mannini, M.; Sessoli, R. Magnetic Bistability of a TbPc2 Submonolayer on a Graphene/SiC(0001) Conductive Electrode. *Nanoscale* **2018**, *10* (6), 2715−2720.
(30) Zhu, Y.; Yang, J.; Zhang, S.; Mokhtar, S.; Pei, J.; Wang, X.; Lu, Y. Strongly Enhanced Photoluminescence in Nanostructured Monolayer MoS2 by Chemical Vapor Deposition. *Nanotechnology* **2016**, *27* (13), 135706.
(31) Souto, J.; de Saja, J. A.; Aroca, R.; Rodríguez, M. L. Langmuir-Blodgett and Vacuum Sublimed Films of Terbium Bisphthalocyanine. *Synth. Met.* **1993**, *54* (1−3), 229−235.
(32) Cirera, B.; Matarrubia, J.; Kaposi, T.; Giménez-Agulló, N.; Paszkiewicz, M.; Klappenberger, F.; Otero, R.; Gallego, J. M.; Ballester, P.; Barth, J. v.; Miranda, R.; Galán-Mascarós, J. R.; Auwärter, W.; Ecija, D. Preservation of Electronic Properties of Double-Decker Complexes on Metallic Supports. *Phys. Chem. Chem. Phys.* **2017**, *19* (12), 8282−8287.
(33) Pedrini, A.; Poggini, L.; Tudisco, C.; Torelli, M.; Giuffrida, A. E.; Bertani, F.; Cimatti, I.; Otero, E.; Ohresser, P.; Sainctavit, P.; Suman, M.; Condorelli, G. G.; Mannini, M.; Dalcanale, E. Self-Assembly of TbPc2 Single-Molecule Magnets on Surface through Multiple Hydrogen Bonding. *Small* **2018**, *14* (5), 1702572.
(34) Palmgren, P.; Nilson, K.; Yu, S.; Hennies, F.; Angot, T.; Nlebedim, C. I.; Layet, J.; Le Lay, G.; Gothelid, M. Strong Interactions in Dye-Sensitized Interfaces. *J. Phys. Chem. C* **2008**, *112* (15), 5972−5977.
(35) Choi, J.; Zhang, H.; Choi, J. H. Modulating Optoelectronic Properties of Two-Dimensional Transition Metal Dichalcogenide Semiconductors by Photoinduced Charge Transfer. *ACS Nano* **2016**, *10* (1), 1671−1680.
(36) McCreary, K. M.; Hanbicki, A. T.; Sivaram, S. v.; Jonker, B. T. A- and B-Exciton Photoluminescence Intensity Ratio as a Measure of Sample Quality for Transition Metal Dichalcogenide Monolayers. *APL Mater.* **2018**, *6* (11), 111106.
(37) Rao, R.; Islam, A. E.; Singh, S.; Berry, R.; Kawakami, R. K.; Maruyama, B.; Katoch, J. Spectroscopic Evaluation of Charge-Transfer Doping and Strain in Graphene/ MoS2 Heterostructures. *Phys. Rev. B* **2019**, *99* (19), 195401.
(38) Han, T.; Liu, H.; Wang, S.; Chen, S.; Li, W.; Yang, X.; Cai, M.; Yang, K. Probing the Optical Properties of MoS2 on SiO2/Si and Sapphire Substrates. *Nanomaterials* **2019**, *9* (5), 740.
(39) Michail, A.; Delikoukos, N.; Parthenios, J.; Galiotis, C.; Papagelis, K. Optical Detection of Strain and Doping Inhomogeneities in Single Layer MoS2. *Appl. Phys. Lett.* **2016**, *108* (17), 173102.
(40) Rice, C.; Young, R. J.; Zan, R.; Bangert, U.; Wolverson, D.; Georgiou, T.; Jalil, R.; Novoselov, K. S. Raman-Scattering Measurements and First-Principles Calculations of Strain-Induced Phonon Shifts in Monolayer MoS2. *Phys. Rev. B* **2013**, *87* (8), 813071.
(41) Wu, H.; Si, H.; Zhang, Z.; Kang, Z.; Wu, P.; Zhou, L.; Zhang, S.; Zhang, Z.; Liao, Q.; Zhang, Y. All-Inorganic Perovskite Quantum Dot-Monolayer MoS2Mixed-Dimensional van Der Waals Heterostructure for Ultrasensitive Photodetector. *Adv. Sci.* **2018**, *5* (12), 1801219.
(42) Jares-Erijman, E. A.; Jovin, T. M. FRET Imaging. *Nat. Biotechnol.* **2003**, *21* (11), 1387−1395.
(43) Haider, G.; Usman, M.; Chen, T. P.; Perumal, P.; Lu, K. L.; Chen, Y. F. Electrically Driven White Light Emission from Intrinsic Metal-Organic Framework. *ACS Nano* **2016**, *10* (9), 8366−8375.
(44) Zeng, H.; Dai, J.; Yao, W.; Xiao, D.; Cui, X. Valley Polarization in MoS 2 Monolayers by Optical Pumping. *Nat. Nanotechnol.* **2012**, *7* (8), 490−493.
(45) Mak, K. F.; He, K.; Shan, J.; Heinz, T. F. Control of Valley Polarization in Monolayer MoS2 by Optical Helicity. *Nat. Nanotechnol.* **2012**, *7* (8), 494−498.
(46) Tornatzky, H.; Kaulitz, A. M.; Maultzsch, J. Resonance Profiles of Valley Polarization in Single-Layer MoS2 and MoSe2. *Phys. Rev. Lett.* **2018**, *121* (16), 1−5.
(47) Mueller, T.; Malic, E. Exciton Physics and Device Application of Two-Dimensional Transition Metal Dichalcogenide Semiconductors. *npj 2D Mater. and Appl.* **2018**, *2* (1), 1−12.
(48) Vitali, L.; Fabris, S.; Conte, A. M.; Brink, S.; Ruben, M.; Baroni, S.; Kern, K. Electronic Structure of Surface-Supported Bis-(Phthalocyaninato) Terbium(Lll) Single Molecular Magnets. *Nano Lett.* **2008**, *8* (10), 3364−3368.
(49) Schwöbel, J.; Fu, Y.; Brede, J.; Dilullo, A.; Hoffmann, G.; Klyatskaya, S.; Ruben, M.; Wiesendanger, R. Real-Space Observation of Spin-Split Molecular Orbitals of Adsorbed Single-Molecule Magnets. *Nature Comm.* **2012**, *3*, 953.
(50) Yoshino, K.; Lee, S. B.; Sonoda, T.; Kawagishi, H.; Hidayat, R.; Nakayama, K.; Ozaki, M.; Ban, K.; Nishizawa, K.; Ohta, K.; Shirai, H. Optical Properties of Substituted Phthalocyanine Rare-Earth Metal Complexes. *J. Appl. Phys.* **2000**, *88* (12), 7137−7143.
(51) Pederson, R.; Wysocki, A. L.; Mayhall, N.; Park, K. Multireference Ab Initio Studies of Magnetic Properties of Terbium-Based Single-Molecule Magnets. *J. Phys. Chem. A* **2019**, *123* (32), 6996−7006.

https://doi.org/10.1021/acsnano.2c08320
ACS Nano 2023, 17, 2170−2181

(52) Adamo, C.; Barone, V. Toward Reliable Density Functional Methods without Adjustable Parameters: The PBE0Model. *J. Chem. Phys.* **1999**, *110* (13), 6158−6170.
(53) Maialle, M. Z.; de Andrada e Silva, E. A.; Sham, L. J. Exciton Spin Dynamics in Quantum Wells. *Phys. Rev. B* **1993**, *47*, 15776.
(54) Glazov, M. M.; Ivchenko, E. L.; Wang, G.; Amand, T.; Marie, X.; Urbaszek, B.; Liu, B. L. Spin and Valley Dynamics of Excitons in Transition Metal Dichalcogenide Monolayers. *Phys. Stat. Sol. (B) Bas. Res.* **2015**, *252* (11), 2349−2362.
(55) Slobodeniuk, A. O.; Basko, D. M. Exciton-Phonon Relaxation Bottleneck and Radiative Decay of Thermal Exciton Reservoir in Two-Dimensional Materials. *Phys. Rev. B* **2016**, *94* (20), 2054231.
(56) Robert, C.; Lagarde, D.; Cadiz, F.; Wang, G.; Lassagne, B.; Amand, T.; Balocchi, A.; Renucci, P.; Tongay, S.; Urbaszek, B.; Marie, X. Exciton Radiative Lifetime in Transition Metal Dichalcogenide Monolayers. *Phys. Rev. B* **2016**, *93* (20), 2054231.
(57) Lorchat, E.; López, L. E. P.; Robert, C.; Lagarde, D.; Froehlicher, G.; Taniguchi, T.; Watanabe, K.; Marie, X.; Berciaud, S. Filtering the Photoluminescence Spectra of Atomically Thin Semiconductors with Graphene. *Nat. Nanotechnol.* **2020**, *15* (4), 283−288.
(58) Branzoli, F.; Carretta, P.; Filibian, M.; Graf, M. J.; Klyatskaya, S.; Ruben, M.; Coneri, F.; Dhakal, P. Spin and Charge Dynamics in [TbPc2]0 and [DyPc 2]0 Single-Molecule Magnets. *Phys. Rev. B* **2010**, *82* (13), 1344011.
(59) Pietsch, U.; Holy, V.; Baumbach, T.High-Resolution X-Ray Scattering From Thin Films to Lateral Nanostructures; Springer: New York, 2004; DOI: 10.1007/978-1-4757-4050-9.
(60) Blum, V.; Gehrke, R.; Hanke, F.; Havu, P.; Havu, V.; Ren, X.; Reuter, K.; Scheffler, M. Ab Initio Molecular Simulations with Numeric Atom-Centered Orbitals. *Comput. Phys. Commun.* **2009**, *180* (11), 2175−2196.
(61) Perdew, J. P.; Burke, K.; Ernzerhof, M. Generalized Gradient Approximation Made Simple. *Phys. Rev. Lett.* **1996**, *77*, 3865.
(62) Vosko, S. H.; Wilk, L.; Nusair, M. Accurate Spin-Dependent Electron Liquid Correlation Energies for Local Spin Density Calculations: A Critical Analysis. *Can. J. Phys.* **1980**, *58*, 1200.
(63) Tkatchenko, A.; Scheffler, M. Accurate Molecular van Der Waals Interactions from Ground-State Electron Density and Free-Atom Reference Data. *Phys. Rev. Lett.* **2009**, *102* (7), 730051.

https://doi.org/10.1021/acsnano.2c08320
ACS Nano 2023, 17, 2170−2181